Nonhydrostatic semi-elastic hybrid-coordinate SISL extension of HIRLAM. Part II: Numerical testing

Rein Rõõm*, Aarne Männik, Andres Luhamaa, Marko Zirk

Institute of Environmental Physics, Tartu University,

Ülikooli 18, 50090 Tartu, Estonia

* Corresponding author

email: Rein.Room@ut.ee

Abstract

The semi-implicit semi-Lagrangian (SISL), two-time-level, non-hydrostatic numerical scheme, based on the non-hydrostatic, semi-elastic pressure-coordinate equations, is tested in model experiments with flow over given orography (elliptical hill, mountain ridge, system of successive ridges) in a rectangular domain with emphasis on the numerical accuracy and nonhydrostatic effect presentation capability. Comparison demonstrates good (in strong primary wave generation) to satisfactory (in weak secondary wave reproduction in some cases) consistency of the numerical modelling results with known stationary linear test solutions. Numerical stability of the developed model is investigated with respect to the reference state choice, modelling dynamics of a stationary front. The horizontally area-mean reference temperature proves to be the optimal stability warrant. The numerical scheme with explicit residual in the vertical forcing term becomes unstable for cross-frontal temperature differences exceeding 30 K. Stability is restored, if the vertical forcing is treated implicitly, which enables to use time steps, comparable with the hydrostatic SISL.

1 Introduction

In a recent paper (Rõõm et al 2006, **PartI** hereafter) we described the architecture, SISL–implementation and numerics of a nonhydrostatic pressure coordinate equation set, so-called MPW model (developed in works by Miller, 1974; Miller and Pearce, 1974; Miller and White, 1984; White, 1989). The numerical scheme was specifically applied in the environment of HIRLAM (Unden et al, 2002) with the aim to generate a numerically efficient non-hydrostatic (**NH**) kernel to this numerical weather prediction model. The developed NH SISL, (i) is a non-hydrostatic model in pressure-based, terrain following hybrid-coordinates; (ii) makes use of a simplified, semi-elastic NH scheme; (iii) presents a semi-Lagrangian advection model, aimed to work at very short scales with grid step 1.0 km and finer; (iv) makes use of the non-isothermal reference state with adaptive, isothermally area-mean reference temperature. All this makes the model rather novel even in comparison with its explicit and semi-implicit Eulerian predecessors (Männik and Rõõm, 2001; Männik et al, 2003), requiring careful check, whether the new scheme is capable of short-scale dynamics modelling, and especially, of short-scale NH effect resolving. In this paper we will report the high-resolution simulation tests with the new numerical model. The applied testing method is rather traditional and is used previously in many investigations (Laprise and Peltier, 1989; Ikawa and Saito, 1991; Pinty et al, 1995; Richie and Tanguay, 1996; Nance and Durrand, 1998; Bouttier, 2002; Schär et al, 2002; Männik et al,

2003; Klemp et al, 2003; Girard et al, 2005). For given orography, the flow is modelled from a nonstationary initial state and boundary fields, both characterised by given, height-dependent reference wind and temperature profiles, until the modelled system – the dry-adiabatic atmosphere – reaches the stationary state with given accuracy. Depending on the area size, wind speed, spatial and temporal resolutions, this may take about hundred to thousand time steps, approximately corresponding to time interval ranging from one to ten hours in the real time-scale. The obtained quasi-stationary solution is then checked against the exact stationary solution, corresponding to the same orography, stratification and boundary conditions. As the numerical modelling experience shows, the traditional use in the role of reference standard of analytical model solutions with constant temperature, stability and wind is not sufficient due to over-simplification of the atmospheric model. Instead, in the current research, the reference standard solutions are obtained by numerically solving the linear discrete wave equation for given optional stratification and wind shear conditions. The solution of this equation, recently developed by Rõõm and Zirk (2006), though numerical, can be treated as an exact reference standard, if solved at sufficiently high spatial resolution. Thus, more different model situations become accessible, and the model quality check gains in reliability.

Another major subject of the investigation in this paper is the stability of the created numerical model. The stability problem becomes actual, as an height-(pressure-)dependent adaptive reference temperature is used in this

numerical scheme, which has been reported previously as a source of instability in the hydrostatic primitive-equation case (Simmons, Hoskins and Burridge, 1978, **SHB78** hereafter). Especially unstable proved to be situations with large negative initial temperature difference from reference state, which occurs, for instance, if the reference temperature corresponds to the tropical troposphere and the initial state is considered an arctic cold temperature distribution. To avoid the instability occurrence, SHB78 proposed to apply a relatively warm isothermal atmosphere for the reference state. This choice has been afterwards applied with success in different hydrostatic, primitive equation based numerical schemes, including the ECMWF model (Ritchie et al 1995) and HIRLAM (McDonald and Haugen, 1993). With the implementation of fully elastic hybrid-coordinate equations (Tanguay et al, 1990; Laprise, 1992; Bubnova et al, 1995), the constant warm reference temperature approximation was reported to be unstable either for 2-time level SISL schemes by Benard (2003), who found that no one reference profile can warrant stability in the fully elastic case and the only solution will be an application of the fully implicit linear sub-system. Later on, the destabilization was found by Benard (2004) to be originating from a systematic negative correlation of explicit parts of gravity and sound wave terms in SISL equations, and the application of two different constant reference temperatures simultaneously in SISL equations was proposed by him as a solution for stability restoration (ibid).

In the light of these investigations, the approach with an height-dependent

reference temperature profile presents rather challenging. However, the linearised with respect to initial temperature fluctuation system, presented in Part I, allowed to suggest that the height-dependent reference temperature might not be a limiting factor in the present model, and the conditional stability of linear sub-model with respect to initial temperature fluctuations was claimed. These claims will be backed up with results of numerical simulations presented in the second half of this paper. The stability investigation is performed, modelling straight geostrophically balanced thermal fronts. Front modelling proves to be a powerful tool for stability study, as it provides analytical initial and boundary condition for numerical model, allowing at that for independent manipulation with cross-frontal temperature contrast and maximum wind speed.

Equations of the Part I will be referred in this paper as (I.#) with # standing for actual equation number.

2 Orographic wave modelling

2.1 Models of orography and atmosphere

The modelling area is a rectangular domain

$$0 \le x \le L_x = N_x \Delta x, \quad 0 \le y \le L_y = N_y \Delta y,$$

with grid of $N_x \times N_y$ of equidistant points $x_i,\ y_j$.

For orography, a 'Witch of Agnesi'-type isolated hill is described with the function

$$h(x,y) = \frac{h_0}{\left[1 + (x-x_0)^2/a_x^2 + (y-y_0)^2/a_y^2\right]^s}\ , \tag{1}$$

where h_0 is the mountain height, $a_x,\ a_y$ are the half-widths of the hill along coordinate axes, and $x_0,\ y_0$ are the coordinates of the hill-centre. Parameter s is either 1.5 or 1. Also an orography is used, proposed by Schär et al (2002)

$$h(x) = h_0 \exp\left[-\left(\frac{x-x_0}{a_x}\right)^2\right] \cos^2\left(\pi \frac{x-x_0}{\lambda}\right) \tag{2}$$

which presents a system of successive mountain ridges, perpendicular to the incoming flow, with the main ridge having height h_0, located at x_0, and secondary ridges on both sides from the main ridge at distances $\pm\lambda$, $\pm 2\lambda$ ..., decreasing in top-heights according to the normal law. In recent years, this profile has gained popularity due to ability to reveal the model quality with respect to numerical accuracy (Schär et al, 2002; Klemp and Skamarock,

2003; Girard et al, 2005).

The model input parameters are pressure-dependent background temperature $T^0(p)$, basic wind profile $U(p)$ and the reference surface pressure, specified parametrically for given orography via barometric formula

$$gh(x,y) = R^0 \int_{\hat{p}_s}^{p_s^0} \frac{T^0(p)}{p} dp,$$

where R^0 is the gas constant of dry air and $p_s^0 = 10^5$ Pa presents the mean sea level pressure.

The initial state is characterised by reference temperature $T^0(p)$ and wind profile $\mathbf{i}U(p)$, where $\mathbf{i}$ is the unit vector in x-direction. The wind profile is taken independent of x, y coordinates initially and then adjusted to a mass-balanced initial wind profile $\mathbf{V}(x,y,p)$, satisfying condition

$$\nabla \cdot \int_0^{\hat{p}_s} \mathbf{V} dp = 0.$$

The adjustment procedure is described in (Männik and Rõõm, 2001).

Profiles $\mathbf{V}(x,y,p)$ and $T^0(p)$ also serve as boundary fields, specifying the flow conditions at lateral boundaries.

The used initial wind and reference temperature profiles together with the corresponding Brunt-Väisälä frequencies are presented in Fig. 1. Temperature model T1 is the isothermal atmosphere case with $T^0 = T_s = 280\ K$ and constant $N = g/\sqrt{c_p T_s} = 0.018\ s^{-1}$. Model T2 describes an atmosphere

with constant $N = 0.01\ s^{-1}$. Temperature profile $T3$ corresponds to the constant ratio $T^0_*(p)/T^0(p)$, where $T^0_*(p)$ is the 'stability' temperature (see Part I). Model T4 is based on experimentally sounded temperature profile (Shutts and Broad, 1993) and used in several numerical modelling studies (Nance and Durran, 1998; Bouttier, 2002, Männik 2003). The wind profile U3 (Fig. 1c) is also based on the same experimental sounding. Other two profiles present constant 10 $m\ s^{-1}$ wind (U1) and 25 $m\ s^{-1}$ wind (U2).

The adiabatic model NH SISL HIRLAM is launched from initial conditions, described above, and modelled until a quasi-stationary limiting flow regime is achieved. This stationary state is then checked against an appropriate exact stationary solution of the corresponding linear model. To have results, comparable with linear solution, the mountain height h_0 must be chosen moderate (< 300 m), though qualitative coincidence is observable up to h_0 $= 1$ km (but the small slant condition $h_0/a_x \leq 0.1$ must be maintained in all cases). For the reference, exact stationary solutions of the discrete (in the spirit of SISL-scheme) linear model (Rõõm and Zirk, 2006) are applied.

2.2 Modelling of quasi-stationary buoyancy waves

Experiments with different atmospheric and orographic conditions are presented in following. The purpose of these experiments is to demonstrate that the developed adiabatic NH SISL scheme gives reliable results and catches all nonhydrostatic phenomena properly. General features, common to all

following experiments with NH SISL model, are (i) absence of any sponge layer on the top, (ii) weak fourth-order spectral filtration with 0.1 smoothing level (the standard level 1 corresponding to damping of the highest spectrally resolved horizontal disturbances at each time step by factor two), (iii) use of zero-level decentering, $\varepsilon = 0$ (see Part I) at time-averaging procedures. Exception is a particular experiment, where the damping influence of $\varepsilon > 0$ will be investigated especially.

2.2.1 Hydrostatic flow tests

In the first experiment, presented in Figure 2, the mountain is an one-dimensional ridge (1) with height $h_0 = 250\ m$ and half-widths $a_x = 30\ km$, $a_y = \infty$. The atmosphere is considered isothermal with $T = T_s = 280\ K$, $N = g/\sqrt{c_p T_s} = 0.018\ s^{-1}$ and the wind is constant $U = 25\ m\ s^{-1}$, ie. the atmospheric model is T1U2 in Fig. 1.

A dimensionless parameter Nh/U is often used (Laprise and Peltier, 1989; Baines, 1995) to characterise the flow properties. In the current case $Nh/U = 0.18$, which is small enough to assume the linearity of the flow. The second well-known parameter Na_x/U is a valid indicator of the nonhydrostatic character of the flow. For the first experiment its value is much larger than 1, which corresponds to the hydrostatic flow regime. Thus, here we deal with the typical linear hydrostatic flow regime. Figure 2 shows the results of 6 hour integrations with (a) NH SISL and (b) HS SISL compared to the analytic solution (c). This is the only example in the present investigation,

where analytical test-solution is applicable without admission, though the numerical linear model would give exactly the same result. The used grid is 114×100 horizontal points with 11 km resolution and 62 levels, which is the HIRLAM doubled 31-level eta-grid, slightly smoothed to avoid oscillation of the layer depth $\Delta\eta_k$ with height.

As it can be seen, the mutual coincidence of the NH and HS numerical models, as well as the coincidence with the analytical solution is perfect in the lower and middle atmosphere. In the upper atmosphere the coincidence is satisfactory as well. The experiment shows that the developed nonhydrostatic model can adequately simulate hydrostatic flows over mountains.

2.2.2 Non-hydrostatic flow tests

In the second experiment, presented in Figure 3, the performance of the model in the linear nonhydrostatic flow regime is investigated. A mountain ridge with 250 m height and the half-widths $a_x = 2.5$ km, $a_y = \infty$ is chosen. The atmospheric model is T3U2 In Fig. 1, i.e the temperature is decreasing, the stability is increasing exponentially with height, while wind remains constant on all levels. The model grid is $206 \times 100 \times 62$ with 550 m horizontal resolution, and the integration time is 1 h. Parameters $Nh/U \sim 0.1$ and $Na_x/U \sim 1$ indicate that the observable flow regime is linear and nonhydrostatic. It can be seen that the NH SISL (panel a) is almost perfect in representing the flow, giving the right location and amplitude of the cells. As expected, in this highly nonhydrostatic regime the HS SISL (Fig. 3b) is not

able to catch the downstream tilt of the wave pattern. Its wave amplitude has a wrong, considerably stronger growth rate with the height than the NH linear model predicts. Due to such strong growth rate, the HS model requires a top sponge layer and intensive horizontal fourth order spectral smoothing. For comparison, the NH SISL does not require any damping on the top at all.

In the model experiment, presented in Figure 4, simulation of the nonhydrostatic flow over a circular hill with $a_x = a_y = 2.5$ km, $h_0 = 250\ m$ is carried out. The atmospheric model (T3U2) as well as the grid parameters are the same as for previous experiment. Panels (a) and (b) in Fig. 4 present simulations from NH SISL and HS SISL, respectively, panel (c) presents the linear stationary solution. The horizontal cross-sections of the vertical wind at 500 hPa are given. As it can be seen, the nonhydrostatic model is close to the linear reference model in the simulation of the nonhydrostatic flow features, though sensible weakening of the wave-amplitude in comparison with test case (c) is already evident on the 500 hPa level. At the same time, the wave pattern of the hydrostatic model (panel b) is completely different, though consistent with the theory of hydrostatic flow.

2.2.3 Experiments with flow over mountain ridge system

In these experiments, the orography is modelled with profile (2), presenting a system of mountain ridges, perpendicular to the main flow. Parameters are chosen equal to those used by Schär et al (2002): $h_0 = 250$ m, $\lambda = 4$

km, $a_x = 5$ km. The atmospheric model is T2U1 in Fig. 1, ie., the model with constant stability $N = 0.01\ s^{-1}$, consistently decreasing with the height temperature, and constant moderate wind $U = 10\ m\ s^{-1}$ throughout the atmosphere. The grid is 276×100 points horizontally, with 550 m grid-step, and the standard HIRLAM 100-level eta-grid in vertical.

Simulation results are presented in Figure 5. In the close vicinity of the mountains, the separate ridges are resolved by flow, which is observable as an intense, vertically oriented, evanescent wave pattern below 700 hPa level. Above that level, the mountains together with the trapped waves are treated by flow as a single bell-shaped orographic feature, generating a slant upward propagating, quasi-hydrostatic wave-train of relatively large amplitude. Below 400 hPa the coincidence between NH SISL HIRLAM and and reference model is quite good. Above 400 hPa level the wave crest locations start to diverge, the NH SISL model places them slightly downs-stream and on the lover levels. At the same time, the wave amplitudes are right. Additional weak secondary waves with $\sim 0.1\ ms^{-1}$ amplitude, propagating up to 50 km distance down-stream from the ridge system centre in the NH SISL model, and 80 km distance in the linear stationary case, are generated by primary waves. In this weak secondary wave pattern, the differences between non-stationary NH SISL model and test case are most remarkable. NH SISL produces some stronger secondary waves in the upper troposphere, observable as the down-stream prolongation of primary hydrostatic waves. The reference model (Fig. 5b) gives only some weak waves in the form of isolated

bubbles in the same area. At the same time, the nonstationary model is not able to reproduce weak pattern at the upper boundary between 80 to 100 km down-stream.

The general conclusion from this model experiment is, that in these rather complex orographic conditions, the NH SISL scheme manages well with primary wave generation but is not sufficiently eager to reproduce weak down-stream secondary waves in the upper troposphere, in creation of which it succeeds qualitatively but not much quantitatively.

2.2.4 Experiments with sounded wind and temperature profiles

The variability of wind with height and the tropopause presence in the temperature profile, manifesting itself in the abrupt jump of the Brunt-Väisälä frequency at the tropopause transition, alters the orographic wave pattern radically. Long, intense, down-stream propagating stationary wave-trains appear in the troposphere.

Modelling of such an elongated, stationary wave pattern from an initially wave-free laminar flow conditions is a rigorous challenge for any nonstationary numerical model in several aspects. First, the down-stream weakening of wave amplitude and shifts in wavelength are sensitive indicators of multiple energy dissipation mechanisms hidden in nonstationary numerical schemes, most of them of numerical rather than physical origin, like the fourth order spectral filtration, the Robert - Asselin (Robert, 1969; Asselin, 1972) time

smoothing, which is usual in leap-frog schemes, application of top sponge layers (second order filtration and/or Rayleigh damping), the multiple interpolations, which are common in SISL schemes, and approximation of trajectory integrals with two-point quadratures with decentering parameter ε, applied optionally also in the current model (see (I.11)). Second, the wave trains, reaching in some cases (assuming a frictionless flow) up to thousand kilometres in longitude, will leave the integration area through lateral boundary. Thus, the boundary relaxation scheme quality will be tested in two aspects: (i) whether it is reflective or not with respect to incident waves, and (ii) how deep into the internal regions of the domain of integration the boundary zone damping influence will reach.

In Fig. 6 , the results of modelling with wind profile U3 and temperature profile T3 are presented. The grid and the resolution is the same as in the previous experiment. The orography is presented by isolated ridge (1) with $h_0 = 100\ m$ and $a_x = 3$ km, $a_y = \infty$. In Fig. 6a, modelling with NH SISL scheme is presented. The integration time step is 50 s, and the integration time is 4 h. In Fig. 6b, the reference solution of stationary linear problem is presented, while Fig. 6c reproduces the results NH SISL again, but the decentering parameter is put $\varepsilon = 0.1$ (in all previous experiments it was zero). Comparison of Fig. 6a to the test solution in Fig. 6b reveals very good coincidence of both models in wave amplitude, wave crest location, and wavelength presentation. However, differences are apparent in the fine structure of waves which increase with the height. In Fig. 6a, a weakening and dissipation

of incident wave in the right-end lateral boundary relaxation zone is apparent, but no reflection and propagation of dissipation into domain outside the boundary relaxation zone is observable. The reference solution (Fig. 6b) gives much longer wave train than shown in figure, spreading about 250 km in longitude and reaching far outside the modelling domain of the NH SISL scheme (151.25 km in present experiment). At the same time, some weak spurious waves are generated at the left top edge of the area and some weak waves are reflected upstream from mountain in Fig. 6a. From Fig. 6c follows, that the nonzero decentering parameter $\varepsilon = 0.1$ is a cause of significant down-stream wave energy dissipation. The purpose of ε is to increase the weight of final state in trajectory integrals, and in this way, to increase the stability of numerical scheme, which is acute, if the initial and boundary data are noisy (typical to real forecast situation). However, as the presented examples reveals, nonzero ε should be avoided, applying rather additional spectral smoothing to initial and boundary data.

3 Numerical stability

3.1 Stability problem

As it was stated in the Part I, the linear sub-model (I.29) of the present SISL scheme proves to be numerically stable for sufficiently short time steps (which was called as the conditional stability), if the reference atmosphere is

hydrostatically stable, $T_*^0 > 0$, and the explicit residual coefficients (I.30a), (I.30c) satisfy conditions $|\varepsilon_\phi| < 1$, $|\varepsilon_\phi| < 1$. It can be expected, that the maximum stable time-step is dependent on these coefficients in the nonlinear numerical scheme, also. In addition, in the moving media, the available time step will be certainly affected by the maximum material speed U_{max} (which determines the maximum Lagrangian trajectory length during a single time-step). However, the size of actual maximum stable time step remains for the nonlinear full scheme open and must be established experimentally.

In SHB78 it was shown that a SISL scheme can prove unstable, if the non-isothermal reference atmosphere is applied, while the actual atmosphere is systematically colder and has an essentially lowered tropopause. Such conditions we shall refer further as the SHB test. We will investigate the numerical stability of the full nonlinear SISL scheme on the SHB test example. However, the experiment set-up is a little tricky, as in our case, a systematic lowering of the initial temperature (i.e. systematic negative initial temperature fluctuation $\widetilde{T}$) from $T^0(p)$ in the whole modelling domain is impossible due to the choice of $T^0(p)$ as the area-mean of actual temperature for fixed p at every instant. We can only reach and study model situations, where one half of the domain is much colder than the other. This assumes a thermal front introduction with systematic change of tropospheric temperature and tropopause height through the front. Then, the atmosphere is much colder and the tropopause is much lower on the one side of the front, where the SHB test conditions become locally relevant.

The dynamical situation build-up is shown in Fig. 7. A front with straight parallel isotherms on all levels and with geostrophic thermal wind $\mathbf{v}_T$, blowing along isotherms, moves as a shape-maintaining body with constant velocity $\mathbf{v}_b$, which is the barotropic geostrophic wind, caused by a constant surface pressure gradient. Thus, the complete velocity of an air particle is formed as the sum of the local thermal wind velocity and front replacement velocity. Numerically, front development inside of the inner rectangle (integration domain) is modelled using the SISL scheme. As the analytical solution is known, it is used for the lateral boundary condition specification.

With front dynamics modelling, another concurring instability mechanism can appear, which is the baroclinic instability. This is essentially different from the numerical instability and manifesting itself in a long-wave, slow bending and deformation of the initially straight front. Such large development can be easily distinguished from the numerical instability, presenting a short-scale noisy pattern. Also, the time scale of baroclinic development is much longer than the numerical instability time scales. In addition, the lateral boundary conditions, fixed in our case via Davies' boundary relaxation scheme, exhibit certain stabilizing effect, preventing from baroclinic instability growth. Thus, in the following modelling experiments with maximum 24 h development time no sensible front bending is fixed, though the numerical scheme actually supports such kind of dynamical instability development.

Temperature profile in the frame, moving with front, is given by formula

$$T(\zeta,\eta) = \max\left\{T_s(\zeta)a(\eta), T_1\right\}, \tag{6}$$

$$T_s(\zeta) = T_0 + \frac{\Delta T_s}{\pi}\mathrm{arctg}(\zeta/\zeta_0), \qquad a(\eta) = Q + (1-Q)\eta^{\varkappa}.$$

where ζ is the distance from the front central axis, $T_s(\zeta)$ is the surface temperature, T_0 =285 K, T_1 = 225 K are the mean surface and constant stratospheric temperatures, respectively, ΔT_s is the surface temperature difference through the front, which is the main variable modelling parameter; ζ_0 = 100 km presents the half-width of the front, whereas parameter Q is chosen from condition $a(\eta_1) = T_1/T_0$, where η_1 = 0.3 is the mean tropopause height in eta-coordinates.

In Fig. 8, (a) temperature profiles and corresponding amplitude factors of the linear model (c) ε_ϕ, and (e) ε_ω in the front with tilted tropopause are shown for ΔT_s = 20 K (referred **Front A** hence on). For comparison, in panels (b), (d), and (f), the corresponding graphs are presented for the same cross-frontal surface temperature difference but with front extinction to the tropopause level with the consequent tilt-free tropopause (**Front B**). $T_C = T(-\infty,\eta)$ and $T_W = T(\infty,\eta)$ in panels (a) and (b) present the ultimate local temperature profiles far from the front central axis, while $T^0(\eta)$ is their average in the role of the area-mean reference temperature. The cross-frontal temperature jump ΔT = 20 K is near the observed maximum in local area models. Thus, the amplitude factors ε_ϕ, ε_ω, which are expectedly the main stability influencers,

give some idea on the maximum size of these parameters in real conditions: $|\varepsilon_\phi|_{max} \sim 0.07$ and $|\varepsilon_\omega|_{max} \sim 0.5$. For comparison, the maximum values for the same temperature distributions, but for isothermal reference state $T_0 =$ 285 K would be $|\varepsilon_\phi|_{max} \sim 0.07$, $|\varepsilon_\omega|_{max} \sim 0.8$. Thus, reference temperature manipulations would affect mostly the size of ε_ω. Note, that ε_ϕ, ε_ω in Fig. 8 present characteristic of the linear model and are explicitly absent in the nonlinear scheme. To $\varepsilon_\phi \to 0$, in nonlinear case the transition from SVF to IVF scheme corresponds.

3.2 Stability experiments

Experimentation shows that model performance and stability properties do not depend on the transitional movement of the front neither on the front orientation. In following, results of the modelling of a steady front, tilted at 45 deg with respect to the x-axis are presented. The grid in this simulation is a 114x100x62 set, with 11 km (0.1 arc degree) horizontal resolution and standard HIRLAM η-distribution. For the resolution effect study, also the 22 and 3.3 km resolutions have been applied in comparative experiments. No top sponge layer is applied; the 4rth order spectral filtration has 0.1 smoothing level. The standard for maximum wind speed, which is reached on the top of front centre, is chosen $\approx$ 100 m/s. The wind speed is manipulated via Coriolis parameter. As an instant, $f = 0.0002$ 1/s gives $u_{max} = 101$ m/s for front A, while $f = 0.0001$ 1/s gives $u_{max} = 102$ m/s for front B.

Fig. 9, panels (a) and (c) show the wind v-component (due to 45 deg angle of the front, cross section of the u-component is identical by absolute value) and fluctuative temperature $\widetilde{T}$ vertical cross-sections along x-axis at $y = 0$ after 24 hour development. The exact (analytical) solutions are indicated with broken lines. Modelling is carried out with SVF scheme. The SVF scheme behaves in this example stably and the solution accuracy is good, though the horizontal temperature difference $\Delta T = 20$ K is quite meaningful. The stability is achieved due to application of sufficiently short time step which is 120 s in this particular example. Modelling with IVF scheme gives the same profiles, but the available time step will be 2.5 times longer, 300 s. Modelling with SVF scheme in non-stable mood with $\Delta t = 180$ s, exceeding the stable time-step limit of SVF scheme, is shown in Fig. 9b and 9d. Short-scale wind and temperature disturbances develop in the central part of the front, while the temperature field becomes noisy also in the stratosphere. With the further time step increase, the instability growth will speed up rapidly. In the case of the constant reference temperature $T^0 = 285$ K, when ε_ϕ takes large positive value in the troposphere on both sides of the front, the SVF scheme becomes unstable even at time step $\Delta t = 10$ s.

The stable behaviour of the SVF scheme in real conditions, including reasonably large temperature differences throughout the integration domain, allowed to apply this model in numerical weather forecast at 3.3 km resolution (Rõõm et al 2006), though the time step gave up in comparison with the hydrostatic model. The forecasting performance showed also reasonably

good quality. However, as recent experimentation in more 'severe' temperature difference conditions has revealed, this scheme becomes unstable, if the cross-frontal reference temperature difference ΔT_s becomes very large. The rapid time step decline starts soon after 20 K threshold is surpassed and Δt becomes zero, i.e., the SVF scheme becomes unstable, if $\Delta T_s > \Delta T_{cr} \sim 30$ K, to which $|\varepsilon_\phi|_{\eta=1} \sim 0.1$, $|\varepsilon_\omega|_{\eta=1} \sim 0.5$ correspond. The exact value of ΔT_{cr} will depends also in some extent on the maximum wind speed. This result exhibited that the SVF scheme possesses conditional stability with condition $\Delta T_s < \Delta T_{cr}$. Though not fatal in local-area modelling with the domain lateral flanks not exceeding 1000 - 1500 km, as ΔT_s remains in common below 10 - 20 K, the associated conditional instability remains dangerous, as there is no guaranty that the critical temperature difference can't be locally surpassed in extraordinary circumstances, despite of the optimum area-mean choice of reference temperature. In addition, the available maximum time-step of SVF scheme remains modest even in the conditions of moderate temperature contrasts < 20 K. Thus, it would be eligible to get rid of the dependence of stability on the cross-area temperature difference ΔT_s.

Numerical modelling shows that the time step size (as a stability measure) is most sensitive with respect to the size of parameter ε_ϕ, which is proportional to ΔT_s in front experiments. In particular, the SVF variant becomes unconditionally stable with respect to size of ΔT_s, if the explicit residual of vertical forcing is nullified in numerical scheme, to which $\varepsilon_\phi \equiv 0$ corresponds in the linear case. By the way, this property agrees with the linear theory prediction

(referenced in Part I) that the system becomes unconditionally stable, if $|\varepsilon_\omega|$ < 1 and $|\varepsilon_\omega| = 0$. Though much less by amplitude than ε_ω, parameter ε_ϕ, i.e. the explicit residual of vertical forcing, turns meanwhile to be the main determinator of stability properties of the scheme. The natural way of the explicit residual elimination in vertical forcing without distortion of physics is to apply the IVF scheme. This modification really removes restrictions to the size of ΔT_s. In Fig. 10, Front A type modelling is shown with the IVF scheme, but in this example, the cross-frontal temperature difference $\Delta T_s =$ 60 K, which is approximately the difference in climatological mean tropical and polar temperatures. The front half-width $\zeta_0 = 200$ km. To maintain the maximum wind speed at 100 m/s level, the Coriolis parameter is chosen $f =$ 0.0003 1/s . Left panels present T and v-component of wind for maximum stable time step, which is 300 s (5 min) in this particular 11 km resolution case. Right panels show unstable behaviour at 7 min time step. The maximum available time-step agrees with the time step of the hydrostatic SISL scheme in similar conditions.

For IVF the best choice of T^0 still remains the area-mean (I.4), but system stability is not so much sensitive to the moderate departures of the reference temperature from the area-mean distribution, as it was in the case of SVF scheme. As an example, the warm isothermal reference atmosphere with $T^0 = T_s = 285$ K provides still a stable profile, yet causes a 25 % decrease of the maximum time step from 5 to 4 minutes. The maximum available time step in IVF scheme becomes roughly independent of temperature contrast

ΔT. Another important property of the IVF scheme is, that the time step is inversely proportional to the maximum wind-speed. As an example, for maximum wind speed 50 m/s, the maximum time step becomes 9 min. This property was violated in the SVF scheme, also. Finally, in the IVF case, the available maximum time step is roughly inversely proportional to the horizontal resolution, though a certain relative improvement is observable. For instance, a front A experiment like in Fig. 9 and with the same maximum wind, but on the horizontal resolution $\Delta x = 3.3$ km, gives $\Delta t = 120$ s. Thus, the IVF approach proves to be really effective, as it removes all shortcomings of the former SVF scheme.

As it was pointed in the Part I, the linear theory predicts unconditional stability for the IVF scheme, if $|\varepsilon_\omega| < 1$, and the 'static stability temperature' $T_* = \varkappa T - \eta \frac{\partial T}{\partial \eta}$ remains positive for the reference state: $T_*^0 = \varkappa T^0 - \eta \frac{\partial T^0}{\partial \eta} > 0$. The validity of this condition is easy to prove for the IVF scheme, using the type A front (6), in which case the stability parameter of the actual and reference state troposphere become

$$T_* = Q \varkappa T_s(\zeta), \qquad T_*^0 = Q \varkappa T_s(0).$$

Thus, $Q \to 0$ yields monotonic lowering of stability; the actual initial troposphere and the reference state troposphere become both neutrally stratified for $Q = 0$, and they are unstable for $Q < 0$.

The numerical simulations show that 'in reality' the IVF scheme becomes

unstable immediately before Q becomes zero. For instance, at $\Delta T_s = 30$ K and $U_{max} = 100$ m/s, the instability arises first for $Q = 0.03$, while $Q \geq 0.04$ still maintains stability. That is, the numerical scheme is slightly less stable than the linear theory predicts. Fortunately, a globally neutral troposphere is very artificial, being never observed in reality. If the integration area is large enough so that the actual static stability can vary throughout the domain, being much larger of the critical value ($Q = 0.03$ in the presented instance) in the majority of the area, then the area-mean reference stability will be also larger of the critical value, and the ISF maintains numerical stability. It should be noticed, that locally T_* can become substantially negative in small areas, which will cause the dynamical instability and a local convection generation, while the area-mean reference state will remain stable.

4 Discussion

The modelling with developed semi-elastic NH SISL kernel dynamics with artificial orography and model atmosphere has shown that this model is capable of adequate catching of NH effects. In most cases the coincidence with stationary reference model prediction is quite good. There remain some unsatisfactory results, where the model is not capable of adequate secondary weak wave pattern reproduction, example of which was presented in Fig. 5a. The reason for distortion of secondary waves in this experiment is not completely clear, but indicates, that a further model improvement is possible.

However, this unresolved problem concerns the modelling of marginal secondary wave details. The main wave pattern is modelled rather well, as also demonstrates the modelling with the realistic atmosphere (Fig. 6). Moreover, the generation of primary waves by mountains, responsible for wave energy extraction from the main flow and for consequent wave-drag creation, is modelled coincidently with the reference model.

The stability study, presented in Section 3 of this paper, reveals, that the model stability depends mainly on the usage of the vertical forcing term in the vertical momentum equation. The stability of the SVF scheme , separating vertical forcing to the implicit linear main part and nonlinear explicit residual, is limited to 'mild' cross-area temperature contrasts less than 20 K and disappears completely, if the cross-area temperature difference overpasses 30 K. However, the SVF becomes actually unfit for operational use at 20 K contrast already due to too small time step. The SVF scheme can be applied, if the cross-area temperature contrast does not exceed 5 - 10 K, in which case it even proves computationally more economical than IVF. The dependence of the maximum time-step on the cross-area temperature contrast along with stability loss at large temperature differences present main shortcomings of the SVF scheme.

Concerning the reference temperature choice, the SVF scheme is rather sensitive to it. The most stable profile proves to be the area-mean temperature (I.4). With $T^0(p)$ departure from it, the time step becomes to decrease, while instability arrives at lesser cross-area temperature contrasts. The isothermal

reference temperature proves absolutely unstable (ie. unstable at optionally small time step) at all instances. In this respect the instability in SVF scheme is different from the SHB78 type instability, where stability warrant proved to be just the isothermal profile. Also, the instability in SVF case appears to be insensitive to tropopause tilt. However, some kind of relationship the SVF-type and SHB78-type instabilities possess, as both arrive at large cross-area temperature contrasts.

Contrary to SVF case, the alternative IVF scheme, which treats the nonlinear vertical forcing completely in implicit fashion, proves to be stable independently of the cross-area temperature contrasts and enables time-steps, comparable with the time-step of HS SISL in similar conditions. The IVF scheme is less sensitive to the reference temperature choice, though the area-mean profile (I.4) remains still the most optimal one. As an example, it proves stable with the isothermal reference temperature also, though the 'prise' for that will be 25 % loss in the time step size.

The IVF scheme consumes in adiabatic mode in comparison with SVF case approximately 1.5 times more computational time per single time-step due to the usage of the iterative scheme for omega-equation solution. However, this superfluous time-consumption is in full compensated by the gain in the time-step. At all, this scheme exhibits excellent stability properties independently from the amplitude of the cross-frontal temperature difference, being robust and safe for operational applications.

Acknowledgements.

This investigation has been supported by Estonian Science Foundation under Research Grant 5711.

References

Asselin, R. A. 1972. Frequency filter for time integrations. *Mon. Wea. Rev.*, **100,** 487 – 490.

Baines, P. G. 1995. *Topographic Effects in Stratified Flows.* Cambridge Univ. Press, 482 pp.

Benard P., 2004. On the use of a wider class of linear systems for the design of constant-coefficient semi-implicit time schemes in NWP. *Mon. Wea. Rev.*, **132,** 1319–1324.

Bouttier, F. 2002. Non-hydrostatic dynamical core intercomparisons, Workshop report of HIRLAM Workshop on Mesoscale Modelling, Dublin 14-16 October 2002, 52 – 60, Available from HIRLAM member institutes or http://hirlam.org/open/publications/HLworkshops/mesoscaleDublinOct02

Bubnova R., Hello, G., Bernard, P., and Geleyn, J.-F. 1995. Integration of the fully elastic equations cast in the hydrostatic pressure terrain-following coordinate in the framework of APREGE/Aladin NWP system. *Mon. Wea. Rev.*, **123,** 515 - 535.

Davies, H. C. 1976. A lateral boundary formulation for multilevel prediction models. *Q. J. R. Meteorol. Soc.*, **102**, 405 – 418.

Girard, C., Benoit, R. and Desgagné, M. 2005. Finescale topography and the MC2 dynamics kernel. *Mon. Wea. Rev.*, **133,** 1463-1477.

Ikawa, M. and Saito, K. 1991. Description of a nonhydrostatic model developed at the Forecast Research Department of the MRI. *Technical Reports of the MRI*, **28**, 238 pp.

Klemp, J. B., Skamarock, W. C. and Fuhrer, O. 2003. Numerical consistency of metric terms in terrain-following coordinates. *Mon. Wea. Rev.*, **131,** 1229- 1239.

Laprise, R., 1992: The Euler equations of motion with hydrostatic pressure as an independent variable. *Mon. Wea. Rev.*, **120,** 197 – 207.

Laprise R., and Peltier, W. R. 1989. On the structural characteristics of steady finite–amplitude mountain waves over bell–shaped topography. *J. Atmos. Sci.*, **46,** 586 – 595.

Männik, A. 2003. Implementation and validation of the nonhydrostatic adiabatic core of the numerical weather prediction model HIRLAM. *Dissertationes Geophysicales Universitatis Tartuensis*, 88 pp..

Männik, A. and Rõõm, R. 2001. Non-hydrostatic adiabatic kernel for HIRLAM. Part II: Anelastic, hybrid-coordinate, explicit-Eulerian model. *HIRLAM Technical Report*, **49**, 54p. Available from the HIRLAM member institutes or
http://hirlam.org/open/publications/TechReports/TR49ab.html

Männik, A., Rõõm, R. and Luhamaa, A. 2003. Nonhydrostatic generalization

of a pressure-coordinate-based hydrostatic model with implementation in HIRLAM: validation of adiabatic core. *Tellus*, **55A**, 219 – 231.

McDonald A. 1999. An examination of alternative extrapolations to find the departure point position in a 'two-time-level' semi-Lagrangian integration. *Mon. Wea. Rev.*, **127,** 1985 – 1993.

McDonald A. and Haugen, J.-E. 1993. A two-time-level, three-dimensional, semi-Lagrangian, semi-implicit, limited-area gridpoint model of the primitive equations. Part II: Extension to hybrid vertical coordinates. *Mon. Wea. Rev.*, **121,** 2077 – 2087.

Miller, M. J. 1974. On the use of pressure as vertical co-ordinate in modelling convection. *Q. J. R. Meteorol. Soc.*, **100**, 155 – 162.

Miller, M. J. and Pearce, R. P. 1974. A three-dimensional primitive equation model of cumulonimbus convection. *Q. J. R. Meteorol. Soc.*, **100**, 133 – 154.

Miller, M. J. and White, A.A. 1984. On the nonhydrostatic equations in pressure and sigma coordinates. *Q. J. R. Meteorol. Soc.*, **110**, 515 – 533.

Nance, L. B. and Durran, D. 1998. A modelling study of nonstationary trapped lee waves. Part II: Nonlinearity. *J. Atmos. Sci.*, **55,**1429 – 1445.

Pinty, J.–P., Benoit, R., Richard, E. and Laprise, R. 1995. Simple tests of a semi–implicit semi–Lagrangian model on 2D mountain wave problems.

Mon. Wea. Rev., **123,** 3042 – 3058.

Ritchie, H., Temperton, C., Simmons, A., Hortal, M., Davies, T., Dent, D. and Hamrud, M. 1995. Implementation of the Semi–Lagrangian method in a high–resolution version of the ECMWF forecast model. *Mon. Wea. Rev.*, **123,** 489 – 514.

Richie, H. and Tanguay, M. 1996. A comparison of spatially averaged Eulerian and Lagrangian treatments of mountains. *Mon. Wea. Rev.*, **124,** 167 – 181.

Robert, A. 1969. The integration of a spectral model of the atmosphere by the implicit method. *Proc. WMO/IUGG Symposium on NWP*, Japan Meteorological Society, Tokio, Japan, 19 – 24.

Rõõm, R. and Männik, A. 1999. Response of different nonhydrostatic, pressure-coordinate models to orographic forcing. *J. Atmos. Sci.*, **56,**2553 - 2570.

Rõõm, R., Männik, A. and Luhamaa, A. 2006. Non-hydrostatic, semi-Lagrangian, semi-implicit adiabatic kernel for HIRLAM. Part I: Numerical scheme. *Tellus*, (submitted).

Rõõm R. and Zirk M. 2006. An Efficient Solution Method for Buoyancy-Wave Equation at Variable Wind and Temperature. *Mon. Wea. Rev.*, (Accepted).

Schär, C., Leuenberger, D., Furher, O., Lüthi, D. and Girard, C. 2002. A new terrain-following vertical coordinate formulation for atmospheric prediction models. *Mon. Wea. Rev.*, **130,** 2459 - 2480.

Simmons, A. J., B. J. Hoskins and D. M. Burridge, 1978: Stability of the semi–implicit method of time integration. *Mon. Wea. Rev.*, **106,** 405 – 412.

Tanguay, M., Robert, A. and Laprise, R. 1990. A semi–implicit semi–Lagrangian fully compressible regional model. *Mon. Wea. Rev.*, **118,** 1970 – 1980.

Undén P., Rontu, L., Järvinen, H., Lynch, P., Calvo, J., Cats, G., Cuxart, J., Eerola, K., Fortelius, C., Garcia-Moya, J. A., Jones, C., Lenderlink, G., McDonald, A., McGrath, R., Navascues, B., Nielsen, N. W., Odergaard, V., Rodrigues, E., Rummukainen, M., Rõõm, R., Shattler, K., Sass, B. H., Savijärvi, H., Schreur, B. W., Sigg, R., The, H. and Tijm, A. 2002. HIRLAM-5 Scientific Documentation, *HIRLAM-5 Project, c/o Per Undén SMHI, S-601 76 Norrköping, SWEDEN*, 144 p. Available from the HIRLAM member institutes or http://hirlam.org/open/publications/SciDoc_Dec2002.pdf

White, A. A. 1989. An extended version of nonhydrostatic, pressure coordinate model. *Q. J. R. Meteorol. Soc.*, **115**, 1243 – 1251.

Figure Captions

Figure 1.

Reference profiles of temperature $T^0(p)$, Brunt-Väisälä frequency $N(p)$, and wind $U(p)$, used in model experiments.

Figure 2.

Waves of the vertical velocity field in hydrostatic flow over 2D obstacle. Mountain parameters are $h_0 = 250\ m$ and $a_x = 30\ km$. Isothermal atmosphere with $N = 0.018\ s^{-1}$ and $U = 25\ m/s$ (Model T1 U2). Contour interval is $\Delta w = 0.05\ m/s$. $114 \times 100 \times 62$ grid with 11 km resolution.

Figure 3.

Waves of the vertical velocity field in nonhydrostatic flow over 2D obstacle. Mountain parameters are $h_0 = 250\ m$ and $a_x = 2.5\ km$. Flow with increasing with height N and constant $U = 25\ m/s$ (Model T3 U2). Contour interval is $\Delta w = 0.2\ m/s$. $206 \times 100 \times 62$ grid with 550 m resolution.

Figure 4.

Horizontal cross-section at 500 hPa of the vertical velocity waves in nonhydrostatic flow over 3D obstacle. Mountain parameters are $h_0 = 250\ m$ and $a_x = a_y = 2.5\ km$. Flow with increasing with height N and constant $U = 25\ m/s$ (Model T3 U2). Contour interval is $\Delta w = 0.1\ m/s$. $276 \times 100 \times 62$ grid with 550 m resolution.

Figure 5.

Waves of the vertical velocity field in flow over 2D obstacle consisting of

group of mountains. Mountain group parameters are $h_0 = 250\ m$, $\lambda = 4\ km$ and $a = 5\ km$. Nonisothermal atmosphere with constant $N = 0.01\ s^{-1}$ and $U = 10\ m/s$ (Model T2 U1). Contour interval is $\Delta w = 0.1\ m/s$. $276 \times 100 \times 100$ grid with 550 m resolution.

Figure 6.

Wave train formation in a flow with realistic wind shear and thermal stratification (Model U3 T4). Mountain parameters are $h_0 = 100\ m$ and $a_x = 3\ km$. Contour interval is $\Delta w = 0.05\ m/s$. $276 \times 100 \times 100$ grid with 550 m resolution.

Figure 7.

Scheme of the moving front experiment. Straight lines are the isotherms on an optional fixed η-level. $\nabla_p T'$ and $\mathbf{v}$ are the temperature gradient and thermal wind vectors on this level. The front moves as a rigid body with constant (geostrophic) velocity $\mathbf{v}_g$. Inner rectangle is the integration area, in which front movement is integrated numerically. Boundary fields are obtained from analytical solution.

Figure 8.

Temperature profiles for a front with tropopause tilt (a) , and without tropopause tilt (b). T_c and T_w - temperatures on the cold and warm sides of the front far from the front central axis, T^0 - reference temperature for the area of integration. The mean tropopause height is 300 hPa in both cases. Panels (c) and (d) show the corresponding to (a) and (b) parameter ε_ϕ, (e)

and (f) - parameter ε_ω, for (W) warm and (C) cold area.

Figure 9.

Zonal (y=0) vertical cross sections of the meridional wind component (top panels) and temperature fluctuation (bottom panels) for stable integration mode (left panels, $\Delta t = 120$ s, 24 h development) and for unstable integration mode (right panels, $\Delta t = 180$ s, 6 h development). Tropopause location is marked by the heavy line. Dotted contours mark the exact solution. Isotachs and isotherms are drawn with 5 m/s and 1.0 K interval, respectively.

Figure 10.

Zonal (y=0) vertical cross sections of the meridional wind component (top panels) and temperature fluctuation (bottom panels) for stable integration mode (left panels, $\Delta t = 300$ s, 24 h development) and for unstable integration mode (right panels, $\Delta t = 420$ s, 6 h development). Tropopause location is marked by the heavy line. Dotted contours mark the exact solution. Isotachs and isotherms are drawn with 5 m/s and 2.0 K interval, respectively.

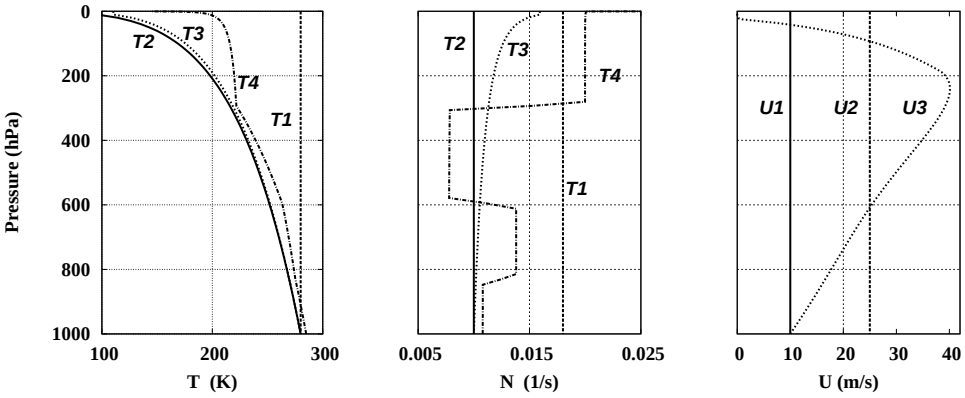

(a) temperature (b) frequency (c) wind

Figure 1: Reference profiles of temperature $T^0(p)$, Brunt-Väisälä frequency $N(p)$, and wind $U(p)$, used in model experiments.

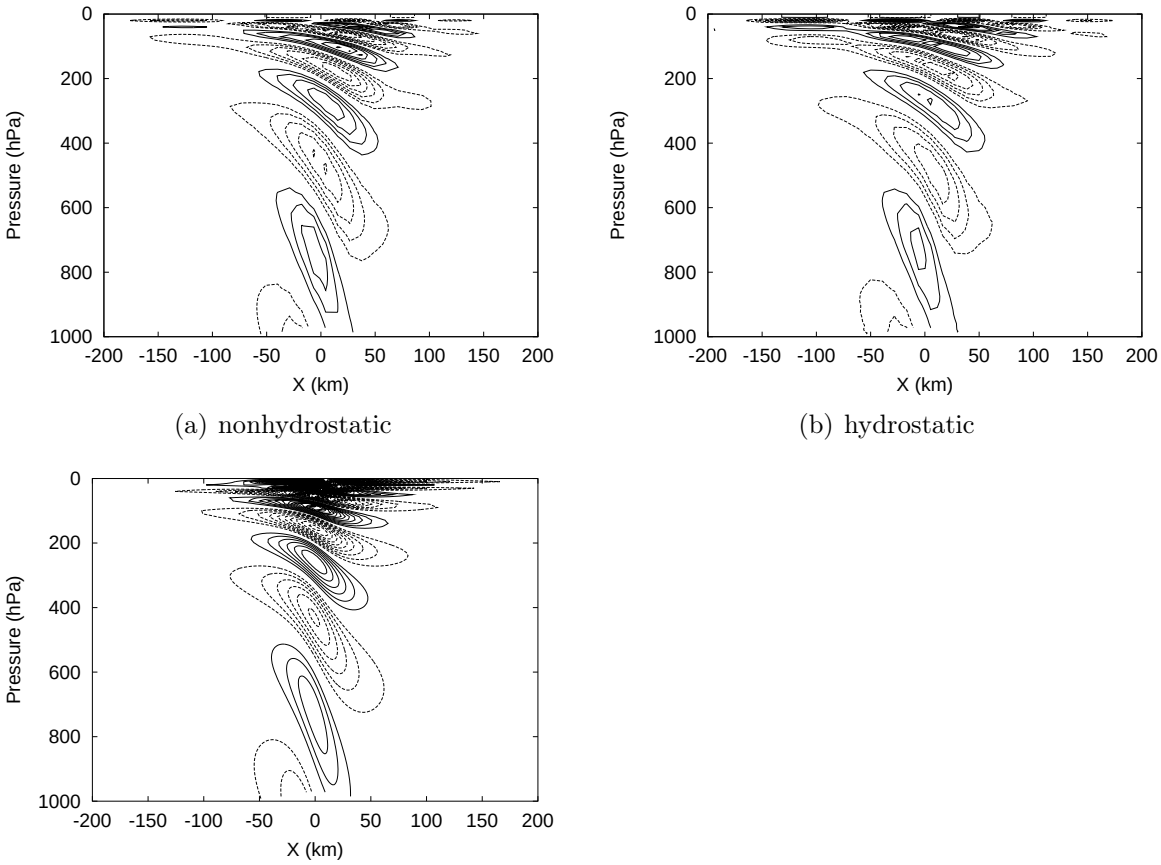

(a) nonhydrostatic

(b) hydrostatic

(c) analytic

Figure 2: Waves of the vertical velocity field in hydrostatic flow over 2D obstacle. Mountain parameters are $h_0 = 250\ m$ and $a_x = 30\ km$. Isothermal atmosphere with $N = 0.018\ s^{-1}$ and $U = 25\ m/s$ (Model T1 U2). Contour interval is $\Delta w = 0.05\ m/s$. $114 \times 100 \times 62$ grid with 11 km resolution.

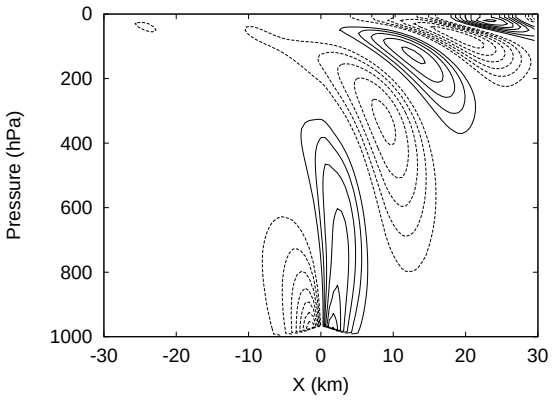

(a) nonhydrostatic

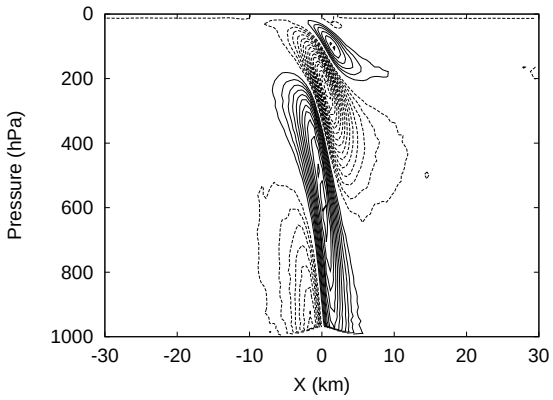

(b) hydrostatic

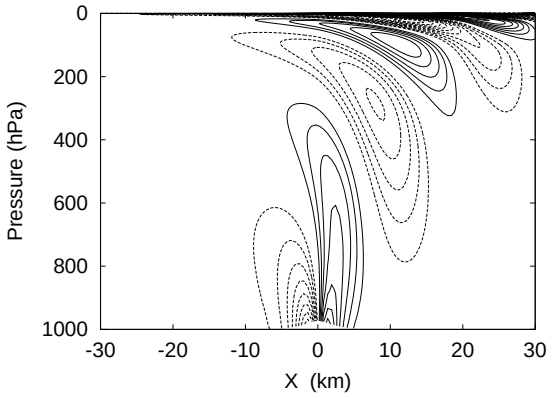

(c) stationary linear

Figure 3: Waves of the vertical velocity field in nonhydrostatic flow over 2D obstacle. Mountain parameters are $h_0 = 250\ m$ and $a_x = 2.5\ km$. Flow with increasing with height N and constant $U = 25\ m/s$ (Model T3 U2). Contour interval is $\Delta w = 0.2\ m/s$. $206 \times 100 \times 62$ grid with $550\ m$ resolution.

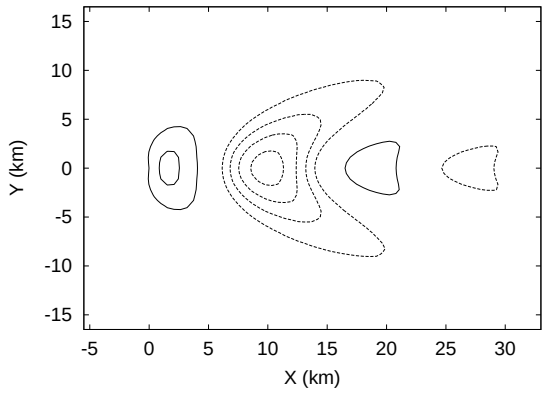

(a) nonhydrostatic

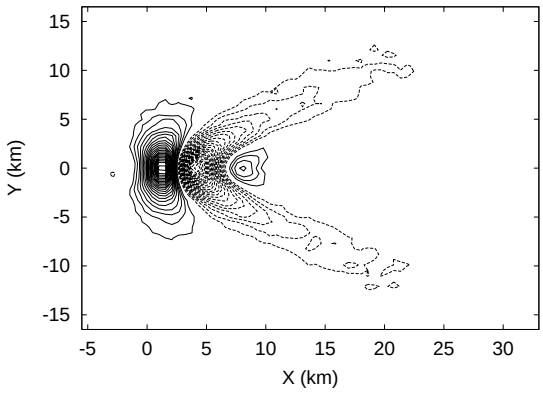

(b) hydrostatic

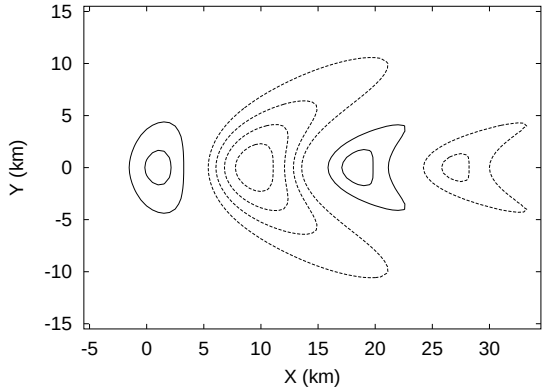

(c) stationary linear

Figure 4: Horizontal cross-section at 500 hPa of the vertical velocity waves in nonhydrostatic flow over 3D obstacle. Mountain parameters are $h_0 = 250\ m$ and $a_x = a_y = 2.5\ km$. Flow with increasing with height N and constant $U = 25\ m/s$ (Model T3 U2). Contour interval is $\Delta w = 0.1\ m/s$. $276 \times 100 \times 62$ grid with 550 m resolution.

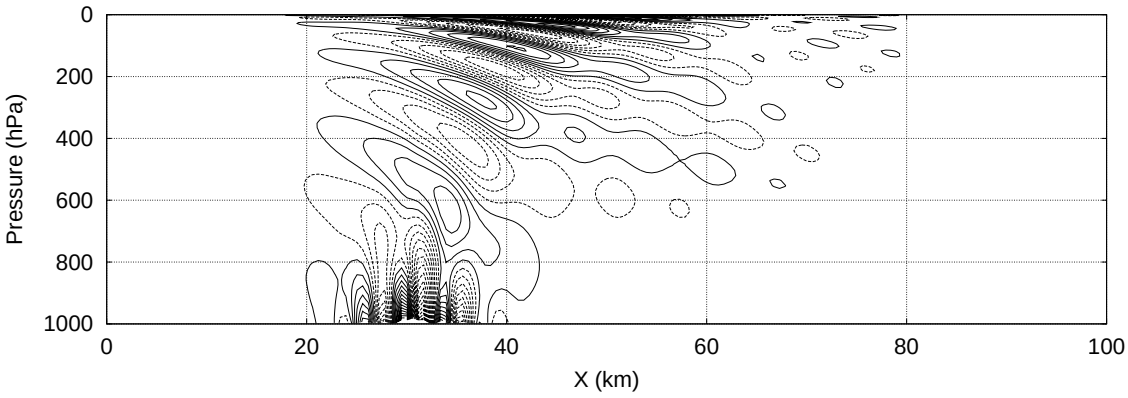

(a) nonhydrostatic

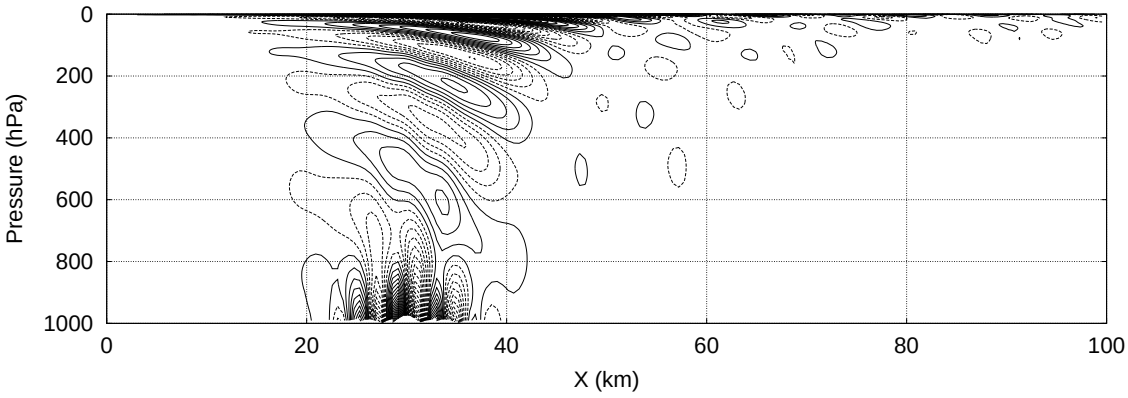

(b) stationary linear

Figure 5: Waves of the vertical velocity field in flow over 2D obstacle consisting of group of mountains. Mountain group parameters are $h_0 = 250\ m$, $\lambda = 4\ km$ and $a = 5\ km$. Nonisothermal atmosphere with constant $N = 0.01\ s^{-1}$ and $U = 10\ m/s$ (Model T2 U1). Contour interval is $\Delta w = 0.1\ m/s$. $276 \times 100 \times 100$ grid with 550 m resolution.

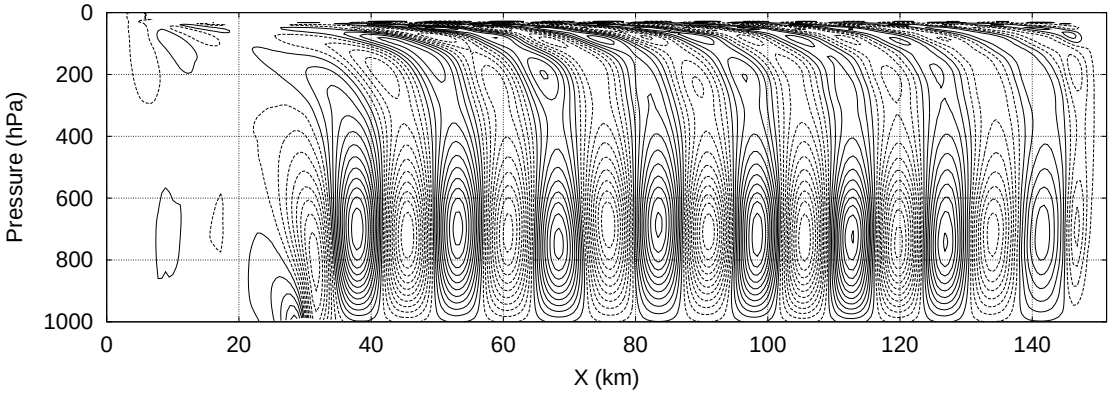

(a) nonhydrostatic

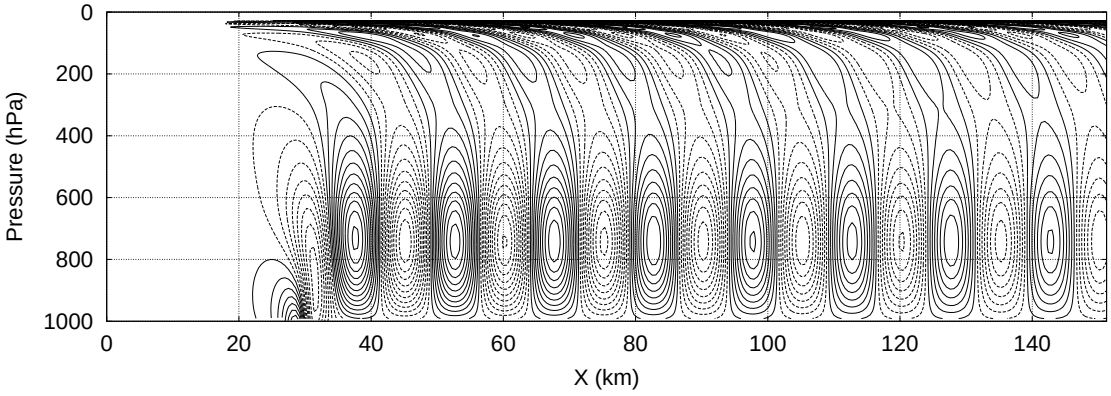

(b) stationary linear

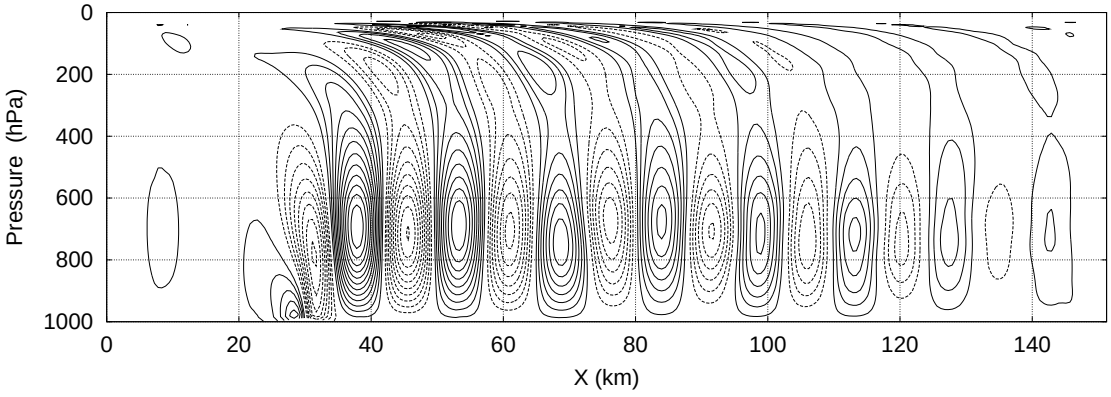

(c) nonhydrostatic, $\varepsilon = 0.05$

Figure 6: Wave train formation in a flow with realistic wind shear and thermal stratification (Model U3 T4). Mountain parameters are $h_0 = 100\ m$ and $a_x = 3\ km$. Contour interval is $\Delta w = 0.05\ m/s$. $276 \times 100 \times 100$ grid with $550\ m$ resolution.

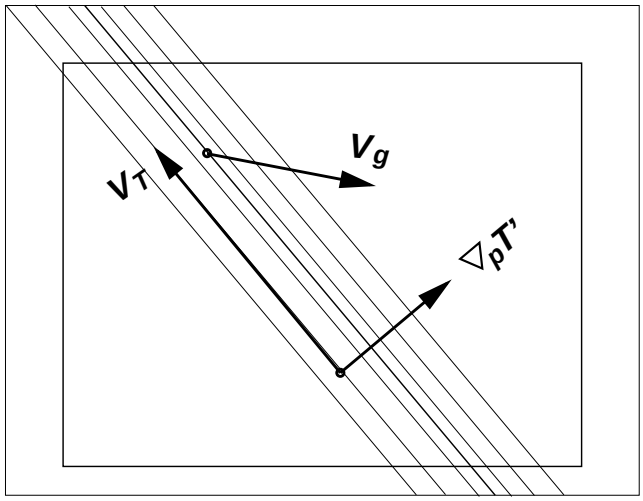

Figure 7: Scheme of the moving front experiment. Straight lines are the isotherms on an optional fixed η-level. $\nabla_p T'$ and $\mathbf{v}$ are the temperature gradient and thermal wind vectors on this level. The front moves as a rigid body with constant (geostrophic) velocity $\mathbf{v}_g$. Inner rectangle is the integration area, in which front movement is integrated numerically. Boundary fields are obtained from analytical solution.

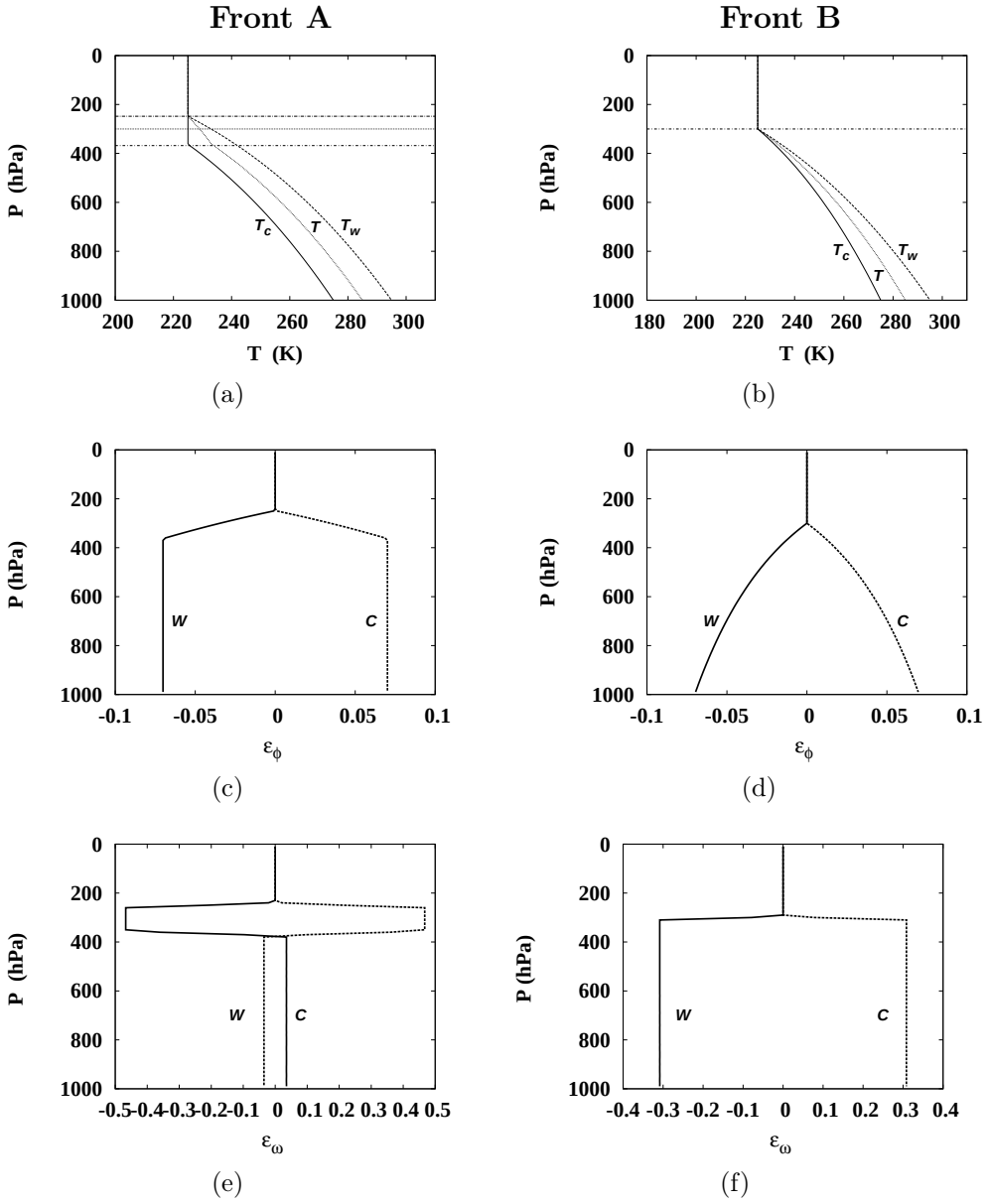

Figure 8: Temperature profiles for a front with tropopause tilt (a) , and without tropopause tilt (b). T_c and T_w - temperatures on the cold and warm sides of the front far from the front central axis, T^0 - reference temperature for the area of integration. The mean tropopause height is 300 hPa in both cases. Panels (c) and (d) show the corresponding to (a) and (b) parameter ε_ϕ, (e) and (f) - parameter ε_ω, for (W) warm and (C) cold area.

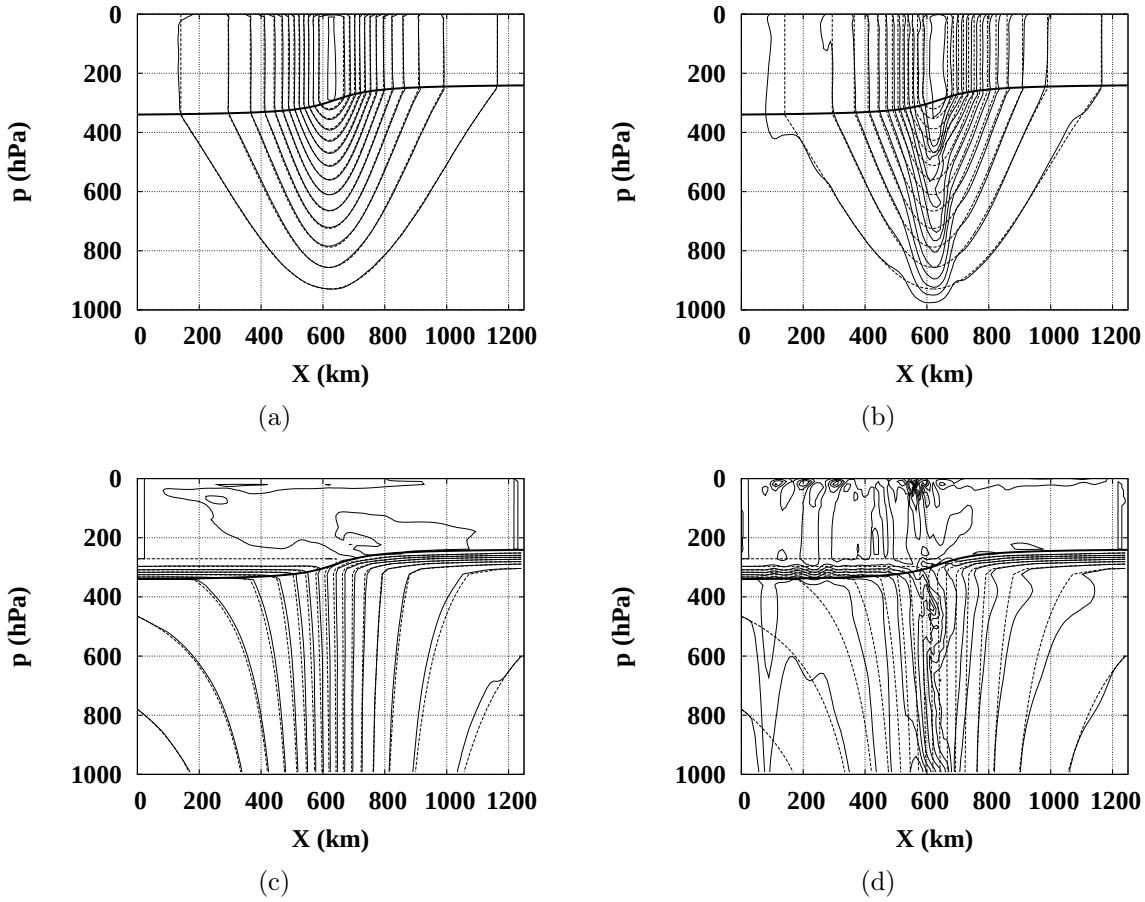

Figure 9: Zonal (y=0) vertical cross sections of the meridional wind component (top panels) and temperature fluctuation (bottom panels) for stable integration mode (left panels, $\Delta t = 120$ s, 24 h development) and for unstable integration mode (right panels, $\Delta t = 180$ s, 6 h development). Tropopause location is marked by the heavy line. Dotted contours mark the exact solution. Isotachs and isotherms are drawn with 5 m/s and 1.0 K interval, respectively.

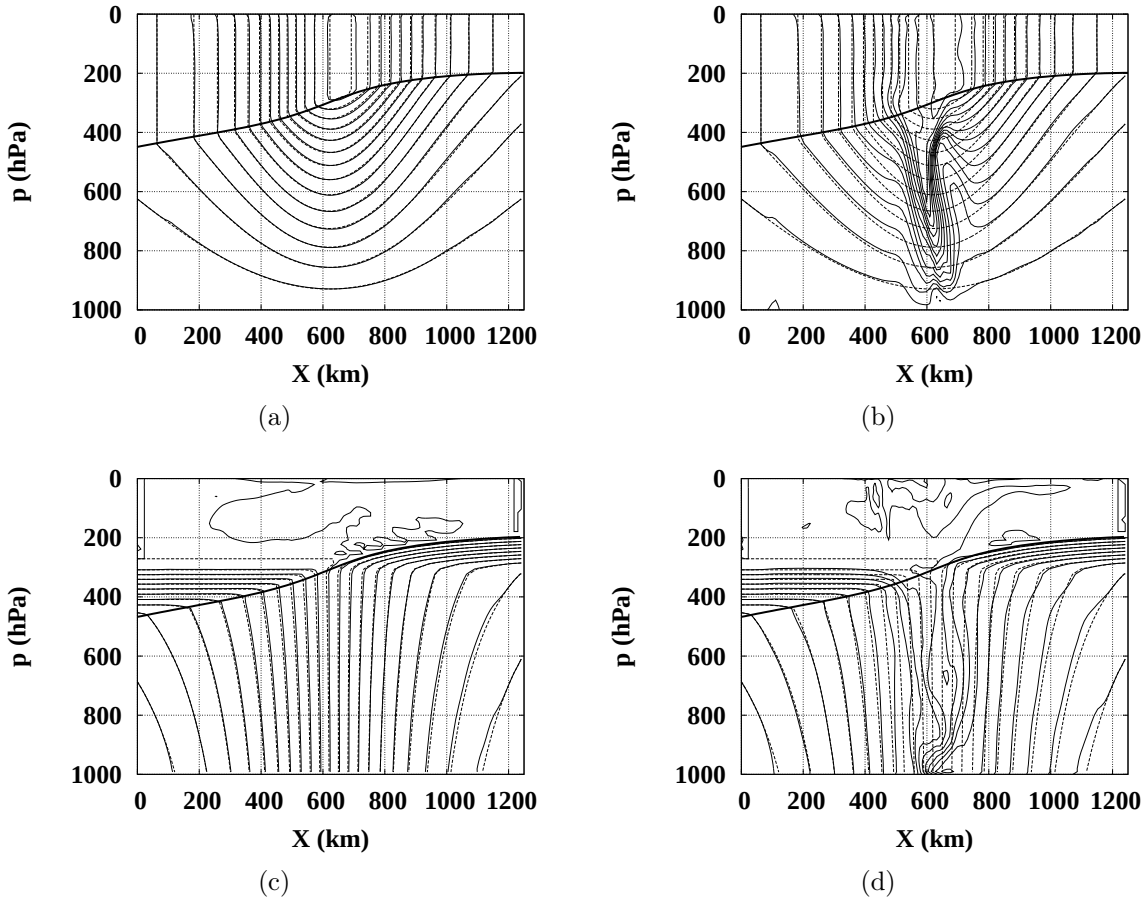

Figure 10: Zonal (y=0) vertical cross sections of the meridional wind component (top panels) and temperature fluctuation (bottom panels) for stable integration mode (left panels, $\Delta t = 300$ s, 24 h development) and for unstable integration mode(right panels, $\Delta t = 420$ s, 6 h development). Tropopause location is marked by the heavy line. Dotted contours mark the exact solution. Isotachs and isotherms are drawn with 5 m/s and 2.0 K interval, respectively.